Accurate Multigrid Solution of the Euler Equations on Unstructured and Adaptive Meshes

Dimitri J. Mavriplis*

NASA Langley Research Center, Hampton, Virginia

A method for accurately solving inviscid compressible flow in the subcritical and supercritical regimes about complex configurations is presented. The method is based on the use of unstructured triangular meshes in two dimensions, and special emphasis is placed on the accuracy and efficiency of the solutions. High accuracy is achieved by careful scaling of the artificial dissipation terms, and by reformulating the inner and outer boundary conditions for both the convective and dissipative operators. An adaptive grid-refinement strategy is presented which enhances the solution accuracy for complex flows. When coupled with an unstructured multigrid algorithm, this method is shown to produce an efficient solver for flows about arbitrary configurations.

Introduction

THE use of unstructured triangular meshes in two dimensions and tetrahedral meshes in three dimensions is becoming more widely accepted as a viable means for computing compressible flows about complex geometries. Various ongoing research efforts in this area can be found in the literature.[1-3] The main advantage of unstructured meshes is that they provide a flexible manner for discretizing topologically complex domains without recourse to large-scale domain decomposition, which is necessary when structured meshes are employed.[4] They also provide a natural setting for the use of adaptive meshing. In fact, previous efforts of adaptive meshing on structured quadrilateral meshes have demonstrated the need for an unstructured-data approach.[5]

On the other hand, unstructured mesh solvers have most often fallen short of their structured mesh counterparts in terms of efficiency and accuracy. The efficiency of these solvers is hindered by the use of indirect addressing required by random data sets, and by generally less efficient solution algorithms. The problem due to indirect addressing can be somewhat alleviated by the use of hardware gather-scatter functions available on an increasing number of present-day supercomputers. Recent work by the author[6,7] has also resulted in an unstructured multigrid algorithm, which has been shown to produce convergence rates comparable to those obtained with current structured mesh solvers. It would thus seem that unstructured mesh solvers are becoming increasingly competitive with structured mesh solvers.

However, the accuracy of unstructured mesh solutions has seldom been able to match that delivered by structured mesh solvers. This issue has in fact been a subject of recent debate. In a recent report, Roe[8] argues that, in general, a piecewise linear discretization of the Euler equations on an arbitrary unstructured mesh results in locally first-order accuracy. Similarly, finite-element proofs of accuracy are most often limited to elliptic equations, and contain constraints on the geometry of the elements. On the other hand, there is much practical evidence indicating that global second-order accuracy can be achieved on unstructured meshes for the Euler equations.[9,10] Although much of the accuracy debate for the Euler equations centers around the discretization of the convective terms on

arbitrary meshes, it is found in practice that the solution accuracy is most significantly affected by 1) The "quality" of the mesh (smoothness, number of connections at a point); 2) The construction of the artificial dissipation terms; and 3) The formulation of the inner and outer boundary conditions.

It is the intent of this work to demonstrate how careful attention to these areas can produce solutions of equivalent accuracy with regards to current structured mesh solvers. An adaptive-meshing procedure is also described, which produces smoothly varying high-resolution meshes. When combined with the unstructured multigrid approach, this method produces efficient and accurate solutions of flows around complex configurations.

Discretization of the Governing Equations

The variables to be determined are the pressure, density, Cartesian velocity components, total energy, and total enthalpy denoted by p, ρ, u, v, E, and H, respectively. Since for a perfect gas we have

$$E = \frac{P}{(\gamma - 1)\rho} + \frac{u^2 + v^2}{2}, \qquad H = E + \frac{P}{\rho} \qquad (1)$$

where γ is the ratio of specific heats, we need only solve for the four variables ρ, ρu, ρv, and ρE. These values are determined by solving the Euler equations, which in integral form read

$$\frac{\partial}{\partial t} \int\!\!\int_\Omega w \, dx dy + \int_{\partial\Omega} (f dy - g dx) = 0 \qquad (2)$$

where Ω is a fixed area with boundary $\partial\Omega$, x and y are Cartesian coordinates, and

$$w = \begin{bmatrix} \rho \\ \rho u \\ \rho v \\ \rho E \end{bmatrix} ; \quad f = \begin{bmatrix} \rho u \\ \rho u^2 + p \\ \rho uv \\ \rho uH \end{bmatrix} ; \quad g = \begin{bmatrix} \rho v \\ \rho vu \\ \rho v^2 + p \\ \rho vH \end{bmatrix} \qquad (3)$$

The w variables are stored at the vertices of each triangle. The control volume for a vertex i is defined as the union of all triangles having a vertex at i, as shown in Fig. 1. The boundary flux integral in Eq. (2) is approximated by first calculating the values of the fluxes f and g at the nodes on the outer boundary of this control volume. These can then be integrated around the control volume boundary by assuming that on each edge, the value of the flux can be taken as the average of the two values on either end of the edge. This corresponds to a finite-volume formulation using the trapezoidal rule of integration.

It can be shown to be equivalent to a piecewise linear Galerkin approximation, with a lumped mass matrix.[1]

Additional dissipative terms are required. These are formulated as a blend of an undivided Laplacian operator in the flow variables, and an undivided biharmonic operator. The biharmonic dissipation is formally third-order accurate on regular meshes and is applied throughout the flowfield. The Laplacian dissipation is formally first-order accurate on regular meshes and is applied only in the vicinity of a shock, where it is needed to prevent oscillations. This adaptive control of the Laplacian dissipation is achieved by multiplying it by a Laplacian of the pressure, which is of order unity near a shock, and remains small elsewhere. This formulation of the dissipation represents an extension of the blended second and fourth differences originally proposed by Jameson et al.[11] Although better shock resolution can be obtained with various upwind-based methods,[3,12] the present formulation is generally better suited for explicit schemes and less expensive to compute. This, in turn, suggests that increased accuracy may otherwise be obtained by adaptive refinement of the mesh in critical areas of the flowfield.

Integration to a Steady State

Discretization of the Euler equations in space transforms the governing equations into a set of coupled ordinary-differential equations that must be integrated in time to obtain the steady-state solution. Thus, Eq. (2) becomes the set

$$S_i \frac{\mathrm{d}w_i}{\mathrm{d}t} + [Q(w_i) - D(w_i)] = 0, \qquad i = 1,2,3,\ldots \qquad (4)$$

where S_i is the area of the control volume i, and is independent of time. The convective operator $Q(w)$ represents the discrete approximation to the flux integral in Eq. (2), and the dissipative operator $D(w)$ represents the artificial dissipation terms. These equations are integrated in time using a fully explicit five-stage hybrid time-stepping scheme, where the operator $Q(w)$ is evaluated at each stage in the time step, and the operator $D(w)$ is only evaluated in the first two stages, and then frozen at that value. Thus, we advance in time as

$$w^{(0)} = w^n$$

$$w^{(1)} = w^{(0)} - \alpha_1 \frac{\Delta t}{S} [Q(w^{(0)}) - D(w^{(0)})]$$

$$w^{(2)} = w^{(0)} - \alpha_2 \frac{\Delta t}{S} [Q(w^{(1)}) - D(w^{(1)})]$$

$$w^{(3)} = w^{(0)} - \alpha_3 \frac{\Delta t}{S} [Q(w^{(2)}) - D(w^{(1)})]$$

$$w^{(4)} = w^{(0)} - \alpha_4 \frac{\Delta t}{S} [Q(w^{(3)}) - D(w^{(1)})]$$

$$w^{(5)} = w^{(0)} - \alpha_5 \frac{\Delta t}{S} [Q(w^{(4)}) - D(w^{(1)})]$$

$$w^{n+1} = w^{(5)} \qquad (5)$$

where w^n and w^{n+1} are the values at the beginning and the end of the nth time step. The standard values of the coefficients are $\alpha_1 = 1/4$, $\alpha_2 = 1/6$, $\alpha_3 = 3/8$, $\alpha_4 = 1/2$, and $\alpha_5 = 1$. This scheme represents a particular case of a large class of hybrid time-stepping schemes, which has been specifically designed to produce strong damping characteristics of high-frequency error modes. This is a desirable property when a multigrid algorithm is to be employed.

The unstructured multigrid algorithm, which has previously been described in detail,[6,7,9] is used to accelerate convergence of the fine-mesh solution to a steady state. This is achieved by repeatedly time-stepping on a sequence of coarse and fine

unstructured meshes. The various meshes of the sequence are assumed to be independent of one another, and the pattern of transferring variables back and forth between the various meshes is determined in a preprocessing stage, where an efficient tree-search algorithm is employed. Convergence to a steady state is also accelerated by using the maximum permissible time step at each point in the flowfield, as determined by local stability analysis, by the use of enthalpy damping[11] and implicit residual averaging.[9]

Formulation of the Dissipation

The artificial dissipation is constructed as a blend of undivided Laplacian and biharmonic operators. For subcritical flow, only biharmonic dissipation is required. This operator is constructed by first forming an approximation to a Laplacian in the flow variables at each node according to

$$dw_i = \sum_{k=1}^n [w_k - w_i] \qquad \text{or} \qquad dw_i = \sum_{k=1}^n w_k - nw_i \qquad (6)$$

w represents the flow variables as given in Eq. (3), with the exception of the last term, where w is taken as the total enthalpy rather than the total energy, in order to preserve a constant total enthalpy in the steady-state solution. k represents the neighbors of node i, the total number of which is n, as shown in Fig. 1. On a Cartesian grid, this corresponds to the standard five-point finite-difference formula. The biharmonic dissipation is then formed by repeating the above step:

$$qw_i = \epsilon_2 \sum_{k=1}^n [dw_k - dw_i] \left(\frac{A_k + A_i}{2} \right) \qquad (7)$$

where ϵ_2 is an empirically determined coefficient, and A_i is given by

$$A_i = \sum_{e=1}^n |u_e \Delta y_e - v_e \Delta x_e| + c_e \sqrt{\Delta x_e^2 + \Delta y_e^2} \qquad (8)$$

The above summation is performed over all edges e, which span the nodes $(k, k+1)$ along the outer boundary of the control volume for node i (cf. Fig. 1). Δx_e and Δy_e represent the x and y increments along edge e. u_e and v_e denote the Cartesian velocity components along the edge, and c_e the speed of sound, which are taken as the average of the values at nodes k and $k+1$, on either end of each edge. This construction of A_i represents the maximum eigenvalue of the Euler equations $|u| + c$ in the direction normal to each control-volume boundary edge, integrated around the boundary of the control volume for node i. This is consistent with the finite-volume formulation and also provides an isotropic value for scaling the dissipation with the maximum local eigenvalue about arbitrarily shaped control volumes. Furthermore, by averaging A_i with A_k, the dissipation is conservative in the w quantities. This can be seen by noting that for each contribution to the summation for node i in Eqs. (6) and (7), an equivalent but opposite term will appear in a similar summation for node k. The Laplacian dissipation required for cap-
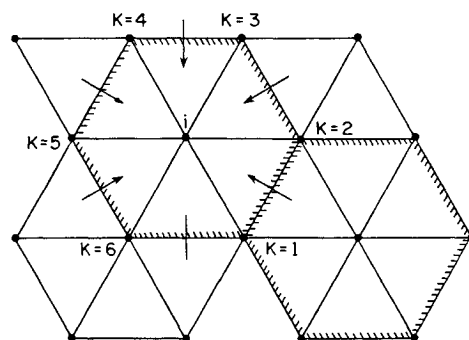

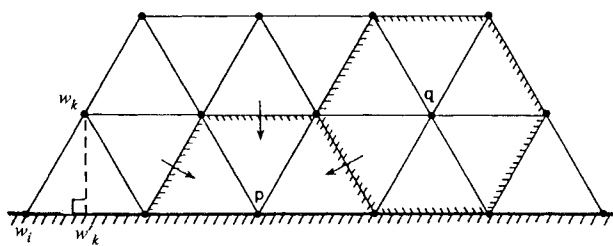Fig. 1 Control volume for vertex triangle scheme.
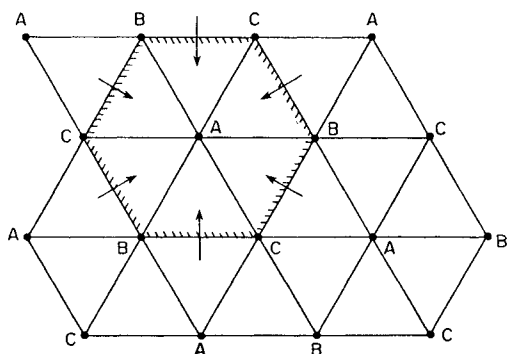
Fig. 2   Control volume for boundary point.

Fig. 3   Three-mode decoupling possible on a regular triangular mesh.

Fig. 4   Partial view of mesh about NACA-0012 airfoil.

turing shocks in supercritical flows is constructed by replacing dw_k and dw_i in Eq. (7) by the flow variables w_k and w_i. To ensure that these dissipative terms are significant only in the vicinity of a shock, the ϵ_2 coefficient is replaced by a scaling proportional to an undivided Laplacian in the pressure:

$$\epsilon_1 \frac{\left| \sum_{k=1}^{n} p_k - p_i \right|}{\sum_{k=1}^{n} p_k + p_i} \qquad (9)$$

Here, ϵ_1 is an empirically determined coefficient taken as $\frac{1}{2}$ for all computations performed in this work. The total dissipation operator is taken as the sum of the Laplacian and the biharmonic terms.

Boundary Conditions

The specific treatment of both convective terms and dissipative terms at both inner and outer boundaries was found to have a significant effect on the solution accuracy. For a vertex scheme, values are computed on the boundaries. The boundary control volumes resemble one-half of a regular inner point control volume, as shown in Fig. 2.

For a vertex discretization of the Euler equations, wall boundary conditions may be applied in several ways. The weak form consists of simply setting the normal components of the f and g fluxes in Eq. (3) to zero, except for the pressure terms in the momentum equations. In this formulation, however, the velocities calculated on the boundary are not necessarily tangential to the wall. A stronger formulation consists of explicitly setting these velocities to be tangential to the wall. However, for a discretized representation of the body, the tangent at a point is ill-defined. In practice, a tangent can be defined as the line connecting the two neighboring boundary points. For curved boundaries on unequally spaced meshes, and for boundaries of varying curvature, this definition of the tangent will yield nonzero fluxes through the faces of the wall. Hence, in addition to setting the velocities tangential to the wall as defined above, the fluxes through the wall are also set to zero. In general, the resulting flux balance for the two momentum equations at the wall will not be satisfied. How-
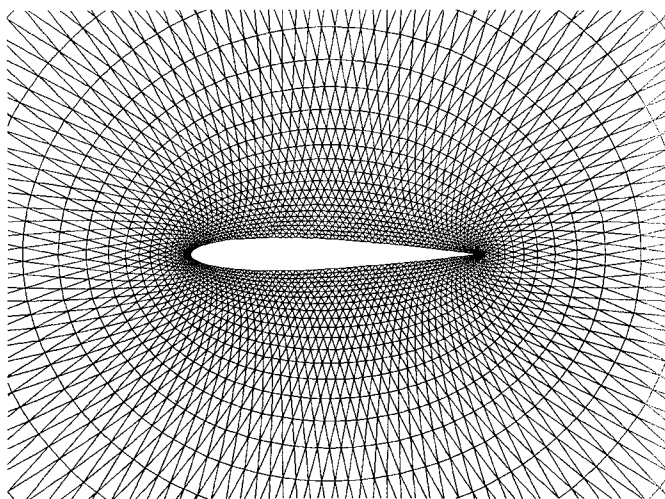
ever, it is the combination of the flux balance and the velocity corrections at the boundary which sum to zero at convergence. In itself, this formulation of the inner boundary condition has only a moderate effect on the solution accuracy. However, the level of dissipation needed to guarantee convergence with this formulation is an order of magnitude smaller than with the weak formulation. It has been found that, as the level of dissipation is lowered, odd-even decoupling of the solution does not occur. Rather, as the convergence degrades, the solution begins to exhibit low-frequency oscillations. Since high-frequency oscillations may be observed on triangular meshes when the weak formulation of the boundary condition is employed, and since they also occur when the strong formulation is employed on quadrilateral meshes, it appears that the combination of the strong formulation and the increased connectivity of the triangular meshes inhibit odd-even decoupling of the solution. In fact, when decoupling is observed with the weak formulation of the boundary condition on triangular meshes, the wall velocity vectors are seen to oscillate about the tangent direction. Furthermore, whereas an odd-even oscillatory mode which exactly satisfies the discretized equations in the interior domain can be found for cell-centered and vertex discretizations on quadrilaterals, and for cell-centered discretizations on triangles,[9] this is not possible for vertex discretizations on triangles. On a regular triangular mesh, as shown in Fig. 3, only a three-mode oscillation pattern can be found for a vertex scheme. In practice, the minimum value of the ϵ_2 coefficient needed to guarantee convergence with the weak formulation was found to be 3/256. With the strong formulation, the value $\epsilon_2 = 1/256$ was found to provide a good compromise between accuracy and speed of convergence, and was thus used for all of the computations performed in this work. Although a direct comparison between this dissipation level and that used in central-difference structured mesh codes is difficult due to the different scalings employed, it is estimated, by examining the levels of numerical entropy production, that this value corresponds to roughly one-half the level of dissipation necessary to guarantee convergence for the structured mesh code.[11]

Treatment of the artificial dissipation terms at the inner boundary can also have a significant effect on the solution accuracy. Large amounts of numerical entropy may be generated in regions of high gradients such as in the rapid expansion on the upper surface of an airfoil at high angles of attack. This false entropy contaminates the solution as it is convected downstream. In particular, when the upper and lower surface flows over an airfoil meet at the trailing edge, large oscillations may occur if one of the flows has an appreciable level of numerical entropy. To help minimize the spurious production of entropy by the boundary dissipation terms, it is convenient

to divide the flow gradients into normal and tangential components at the boundary. For example, this is often achieved with body-fitted quadrilateral meshes where the mesh lines are perpendicular to the body. However, for a triangular mesh, it is impossible to have all mesh lines or edges hitting the boundary either tangentially or normally. Thus, assumptions concerning the local flow gradients at the boundary must be made. In the absence of body curvature, the boundary conditions for the Euler equations imply that the normal derivatives of all quantities at the wall vanish. Hence, it has been assumed that the normal gradient is zero, when computing the artificial dissipation at the wall. Thus, for a mesh edge that intersects the wall at some prescribed angle, the difference $w_k - w_i$ from Eq. (6) is replaced by $w_k' - w_i$, where w_i is the value at the wall, w_k represents the value at the other end of the edge, and w_k' is the value of the point on the wall obtained by projecting node k down onto the boundary, as shown in Fig. 2. The specific value at this point is obtained by linear interpolation between the two points on the wall at either end of this interval. It can be shown that this construction is equivalent to that obtained by omitting the differences in Eq. (6) along all edges intersecting the boundary, and multiplying the differences along the tangential boundary edges by a constant determined by the local grid topology. This modification is only applied to the terms of Eq. (6). The second summation involved in the evaluation of the biharmonic dissipation, i.e., that of Eq. (7), is left unmodified, and is taken as the sum of the differences along all edges that meet at the boundary node i.

Global flow characteristics such as lift and drag coefficients for an airfoil can also be affected by the treatment of the outer boundary. Characteristic boundary conditions have been employed at the far-field boundary. The far-field boundary points of the unstructured meshes are not updated by the time-stepping procedure employed for interior points. Rather, the values at these points are updated by assuming the flow to be locally one-dimensional, and calculating the values at the next time step according to the ingoing and outgoing Rieman invariants for this simplified flow. For the outgoing Rieman invariant, values are extrapolated from neighboring interior points. For the incoming Rieman invariant, flow values are taken as the superposition of the freestream flow with the disturbance flowfield set up by a vortex centered at the quarter-chord point of the airfoil, producing total circulation equal to that of the lifting airfoil.[13] Two other conditions are required for the full two-dimensional Euler flow. These are given by the values of tangential velocity and entropy, which are extrapolated from the interior values for an outflow boundary, and set equal to freestream values, augmented by the vortex flowfield, for an inflow boundary. Dissipation at the outer boundary is treated in the same manner as at the inner boundary, i.e., all normal gradients are assumed to vanish when computing the dissipation terms. This is equivalent to the treatment advocated for cell-centered quadrilateral Euler solvers.

Results on Simple Meshes

The first case considered is a NACA-0012 airfoil with a freestream Mach number of 0.8, and an incidence of 1.25 deg. The mesh employed for this case consists of a regular triangular grid with 4224 nodes, as shown in Fig. 4. The positioning of the nodes is derived from a 128 × 32 quadrilateral O-mesh. This mesh represents the finest of a sequence of four meshes used in the multigrid algorithm to accelerate convergence. The computed surface pressure distribution is shown in Fig. 5. The upper and lower shocks are both well-defined, and no oscillations are visible. The lift and drag coefficients compare well with other inviscid solutions on equivalent and finer quadrilat-
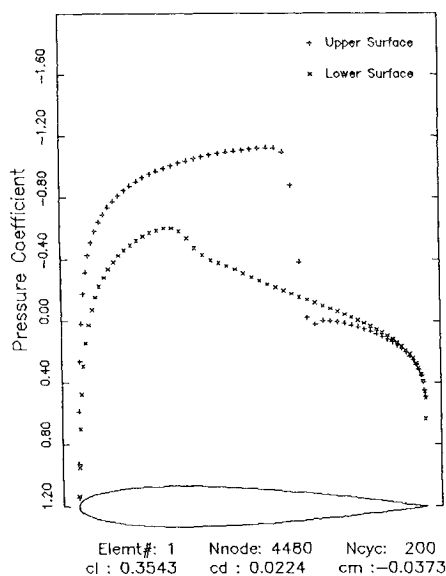
| Elemt#: 1 | Nnode: 4480 | Ncyc: 200 |
| cl : 0.3543 | cd : 0.0224 | cm :−0.0373 |

Fig. 6   Computed surface entropy for NACA-0012 airfoil (M = 0.8, incidence = 1.25 deg).

| Elemt#: 1 | Nnode: 4480 | Ncyc: 200 |
| cl : 0.3543 | cd : 0.0224 | cm :−0.0373 |

Fig. 5   Computed surface pressure distribution for NACA-0012 airfoil (M = 0.8, incidence = 1.25 deg).

Resid1 : 0.12e+01   Resid2 : 0.37e−05   Rate : 0.9381
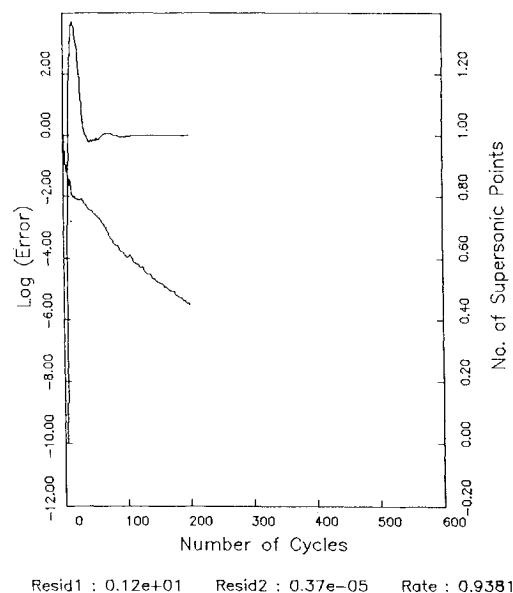
Fig. 7   Convergence history for the supercritical NACA-0012 case.
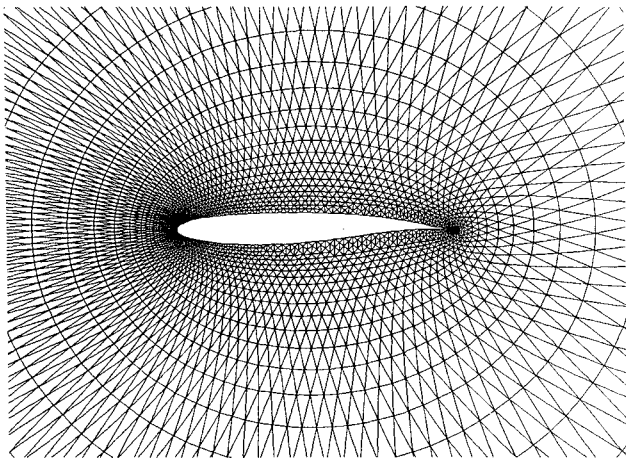
Fig. 8   Partial view of mesh about the Korn airfoil.

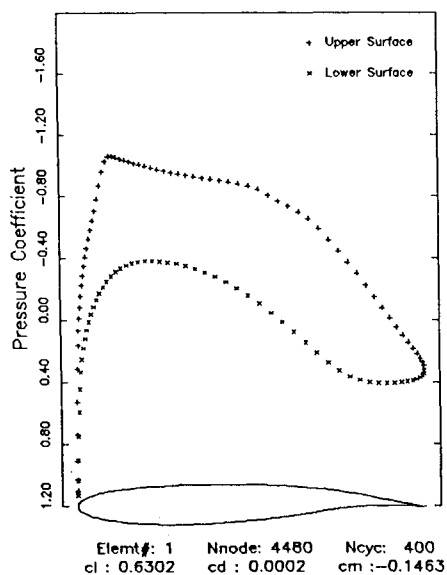Fig. 10   Partial view of unstructured mesh for the Karman-Trefftz airfoil and flap.

Fig. 9   Computed surface pressure distribution for the Korn airfoil at design conditions.

Fig. 11   Comparison of computed surface pressure distribution with analytical incompressible solution for the Karman-Trefftz airfoil and flap.

eral meshes.[14] The surface entropy, which is shown in Fig. 6, is calculated as

$$\frac{p/p_\infty}{(\rho/\rho_\infty)^\gamma} - 1 \qquad (10)$$

The entropy values are nearly zero everywhere ahead of the strong shock, with a maximum value near the leading edge of 0.3%. Behind the upper surface shock, the entropy assumes a constant value as it is convected downstream. The multigrid convergence history given in Fig. 7 indicates a reduction of the rms average of the density residuals of nearly six orders of magnitude over 200 cycles.

The second case is that of a Korn airfoil at design conditions. This airfoil is designed to produce shock-free supercritical flow at these conditions. Since such flows are known to be isolated points (i.e., any change in the geometry or freestream conditions produces a shock), the ability to capture such flows is a good indication of the accuracy of the scheme. The mesh employed corresponds to a 128 × 32 O-mesh and is depicted in Fig. 8. From the computed pressure distribution in Fig. 9, the compression of the flow through the transonic regime can be seen to be gradual. The low drag value (C_d = 0.0002) is an indication of the isentropic nature of the flow, as well as the accuracy of the computed solution.
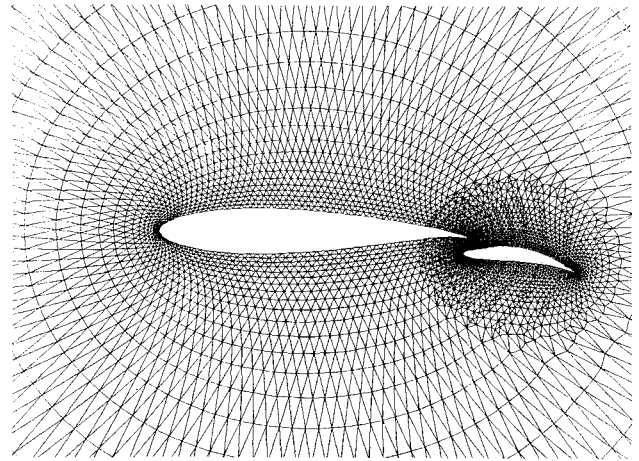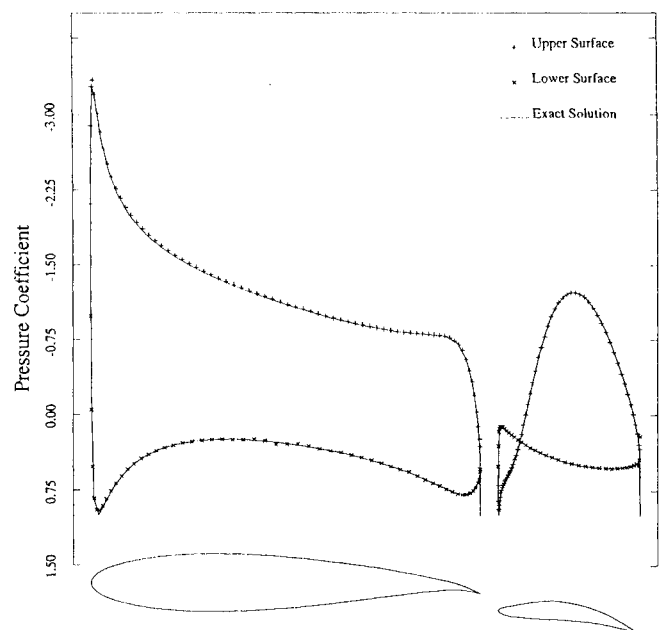
The third case involves flow about a Karman-Trefftz airfoil and flap. An exact incompressible potential solution exists for this case that may be used for comparison purposes. The unstructured mesh about this configuration is shown in Fig. 10. In Fig. 11, the calculated surface pressure distribution is compared with the exact solution. This case was run for a freestream Mach number of 0.125. Hence, effects due to compressibility are small (<1% according to the Prandtl Glauert rule). Good agreement between the two solutions is observed with respect to the surface pressure plots and the calculated force coefficients, which are given in Table 1.

Adaptive-Meshing Strategy

For flows about more complicated geometries, the location of regions where rapid variations in the flow occur are seldom known at the outset. Thus, an adaptive-meshing strategy is necessary to ensure accurate solutions of such flows, as well as to maintain the efficiency of the solver.

The use of adaptive meshing, in conjunction with the unstructured multigrid algorithm, has previously been described in Ref. 7. The method first computes the flow on an existing coarse mesh. A new finer mesh is then constructed by generat-

Table 1 Comparison of computed force coefficients
for the Karman-Trefftz configuration

	Main airfoil		Flap		Total	
	Cl	Cd	Cl	Cd	Cl	Cd
Nodal scheme	1.7005	−0.0906	0.3357	0.0890	2.0362	−0.0016
Analytical incompressible solution	1.6915	−0.0898	0.3366	0.0897	2.0281	−0.0001

ing a new distribution of grid points as determined by the computed flowfield on the coarse grid. These points are then joined together to form an unstructured triangular mesh, using the Delaunay triangulation procedure. Delaunay triangulation is a geometrical construct that represents a unique triangulation of a given set of points in a plane. The resulting mesh is then smoothed by repositioning the mesh points as determined by a Laplacian filtering operation. The patterns for transferring variables back and forth between this new mesh and the previous coarser mesh are determined prior to the solution of the flowfield using a tree-search algorithm. This approach does not assume any relation between the two meshes, thus offering great flexibility in configuring the finer mesh for optimum accuracy. The flow variables are then transferred to the new mesh and time-stepping proceeds, employing the previous mesh as a coarse mesh in the multigrid sequence. This procedure may be repeated, each time generating a new finer mesh, until the desired level of accuracy is achieved. At present, new mesh point distributions are generated by combining all previous mesh points with a set of newly generated points. The distribution of these new mesh points is determined according to a criterion developed by Dannenhoffer and Baron.[15] The first undivided difference of the density along a mesh edge is examined. When this value is larger than some fraction of the rms average of all density differences across the mesh, a new point is added midway along the edge. A second pass is then performed that splits the remaining edges of each triangular element bordering on a previously split edge, thus ensuring an isotropic refinement in these regions. A third pass of this type is also performed on the boundary elements. The mesh-smoothing operation described above displaces the mesh points and thus, in general, the coarse grid points will not coincide with any of the fine grid points. Previous efforts at directional refinement by refining only along edges have met with limited success, due to the nature of Delaunay triangulation, which tends to minimize cell aspect ratios. Other efforts in the literature at directional refinement using alternate triangulation procedures have been more successful.[3]

Results Employing Adaptive Meshes

A subcritical and a supercritical case about a high-lift three-element airfoil configuration were computed using the adaptive-meshing strategy. These solutions were compared with a full-potential flow solver made available by The Boeing Company.[16] This method is a finite-element nonlinear potential flow solver that is formally first-order accurate in supersonic zones, and second-order accurate in subsonic zones. The method operates on a structured quadrilateral mesh, which is generated from a streamline pattern obtained with the aid of a preliminary panel-method solution.

In the subcritical case, the freestream Mach number is 0.2, and the incidence is 8 deg. The final mesh employed in this calculation is shown in Fig. 12. It contains a total of 10745 points, of which 432 are on the airfoil surfaces. This represents the sixth mesh level of the multigrid sequence in which the first two levels are generated globally as described in Ref. 6 and 9, and the four finest levels are generated adaptively. A globally generated mesh of this resolution would have re-
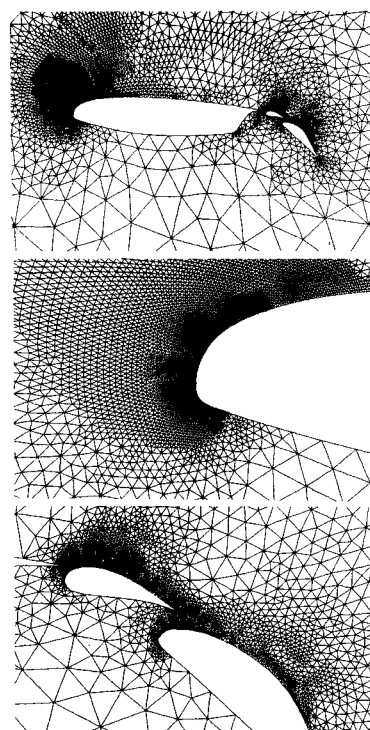

Fig. 12   Illustration of the adaptively refined mesh for the subcritical case of the three-element airfoil configuration (10745 nodes, 20987 triangles).
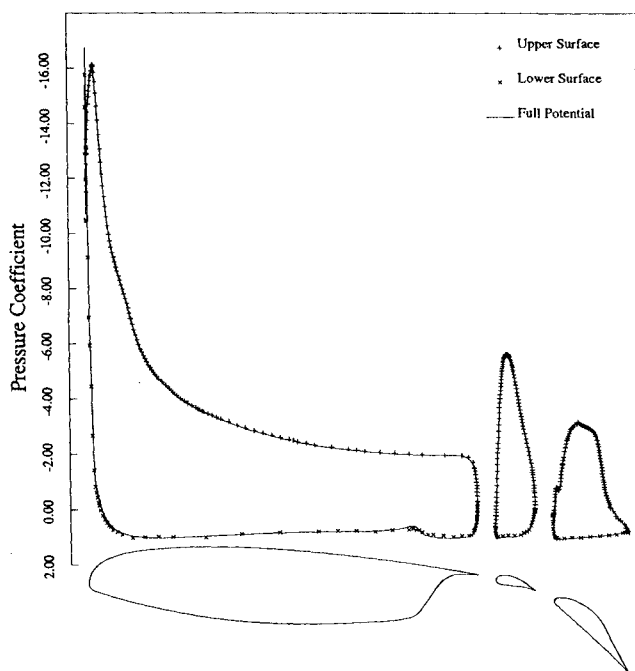

Fig. 13   Comparison of computed surface pressure distribution for the Euler solution with that of the full-potential solution ($M = 0.2$, incidence = 8 deg).

quired 10-20 times more points, and thus would be prohibitively expensive. The computed surface pressure distributions are compared with those obtained by the full-potential solution in Fig. 13. This case exhibits an extreme double suction peak near the leading edge of the main airfoil. Good agreement is observed between the Euler and potential solutions, including the predicted magnitude of the suction peaks. For subcritical cases, the flow should be isentropic, and thus, the plot of the surface entropy in Fig. 14 can be interpreted as a measure of the error in the solution. This entropy is nearly

zero everywhere, except for a region near the leading edge of the main airfoil, where it reaches a peak of 2%. However, throughout most of this region, the entropy is less than 1%. The maximum entropy level could be reduced to less than 1% by employing an additional mesh level. However, the effect on the surface pressure distribution was found to be minimal. The convergence rate for this case is depicted in Fig. 15, where a residual reduction of seven orders of magnitude on the finest mesh was achieved over 300 multigrid cycles, employing all six meshes in the multigrid sequence. A plot of the Mach contours in the flowfield is also given in Fig. 16.

For the supercritical case, the Mach number is increased to 0.25, while the incidence remains 8 deg. At these conditions, the flow becomes supersonic as it expands around the leading

edge of the main airfoil, and a shock is formed. Seven mesh levels were used to compute this solution. The finest mesh is illustrated in Fig. 17, where the highest level of refinement is seen to occur mainly near the leading edge of the main airfoil. The total number of grid points is 12830, of which 539 are on the airfoil surfaces. A convergence of five orders of magnitude over 300 multigrid cycles was achieved for this case, employing seven meshes in the multigrid sequence. The computed surface pressure distribution is shown in Fig. 18, where it is compared to the potential flow solution. The surface entropy, depicted in Fig. 19, rises rapidly through the shock, and then decreases slowly proceeding downstream along the top surface of the main airfoil. Although a constant entropy level behind the shock is expected, it appears that the entropy layer is
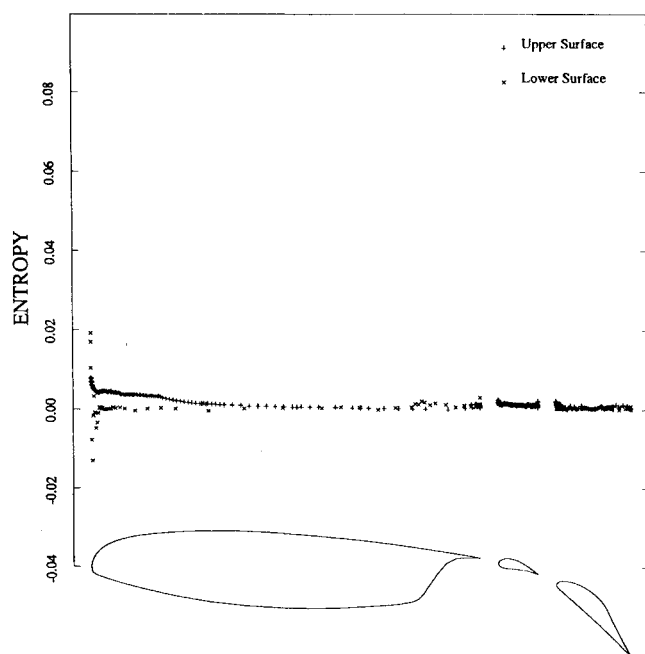

Fig. 14 Computed surface entropy for the supercritical three-element airfoil case ($M = 0.2$, incidence = 8 deg).

Fig. 16 Flowfield Mach contours for the subcritical three-element airfoil case ($M = 0.2$, incidence = 8 deg).

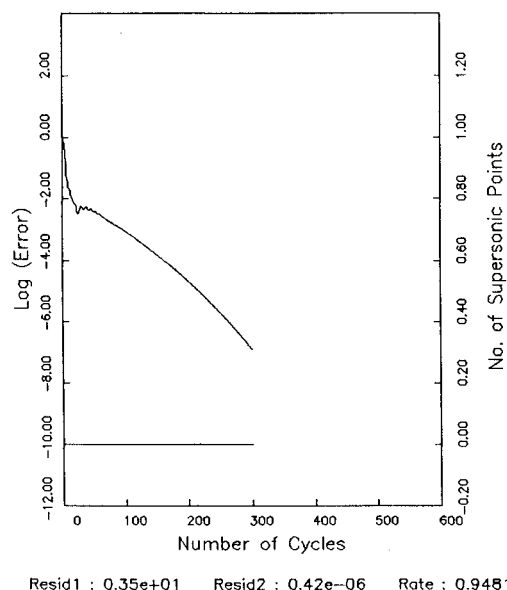
Resid1 : 0.35e+01   Resid2 : 0.42e−06   Rate : 0.9481

Fig. 15 Convergence rate on finest mesh for the subcritical three-element airfoil case as measured by the rms average of the density residual throughout the flowfield.
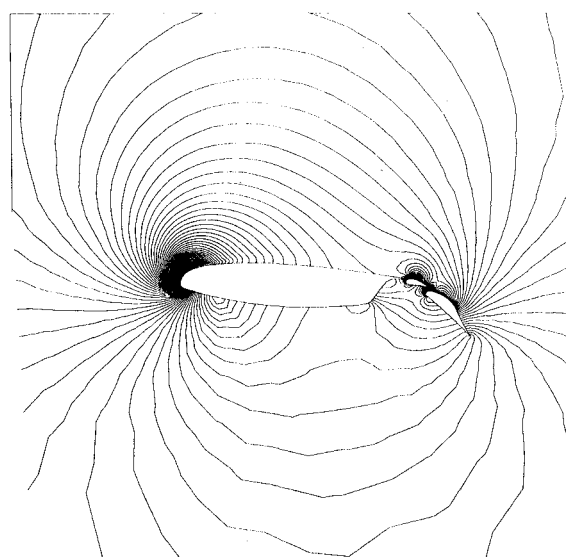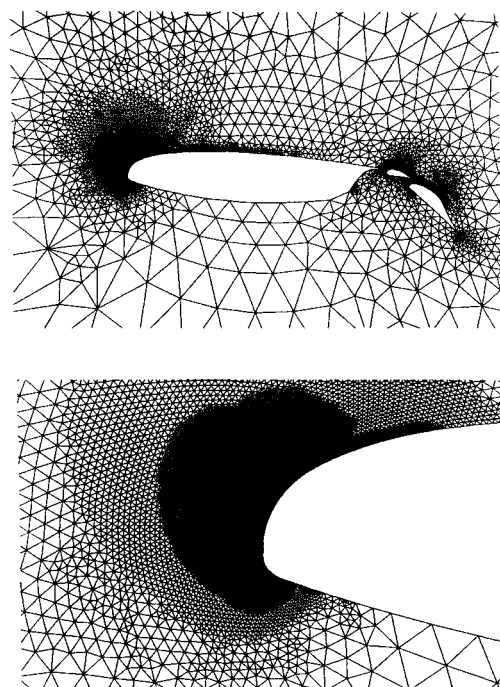

Fig. 17 Illustration of adaptively refined mesh for the supercritical case of the three-element airfoil configuration (12830 nodes, 25125 triangles).
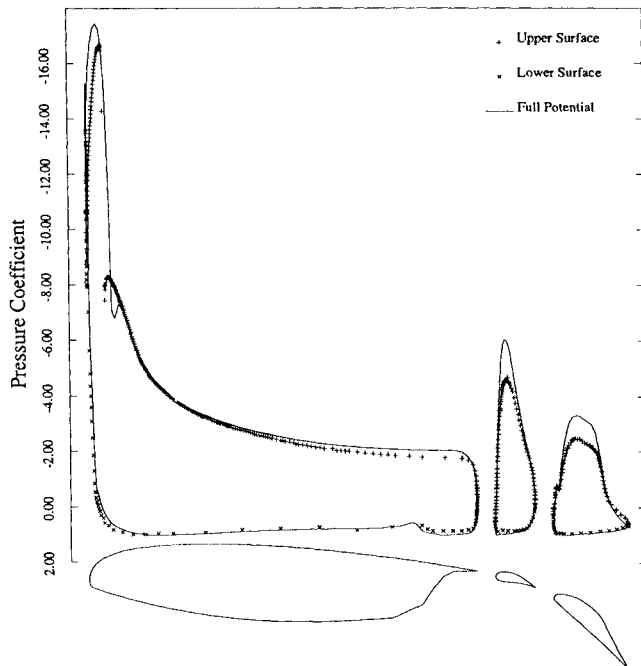
Fig. 18   Comparison of computed surface pressure distribution for the Euler solution with that of the full-potential solution (M = 0.25, incidence = 8 deg).
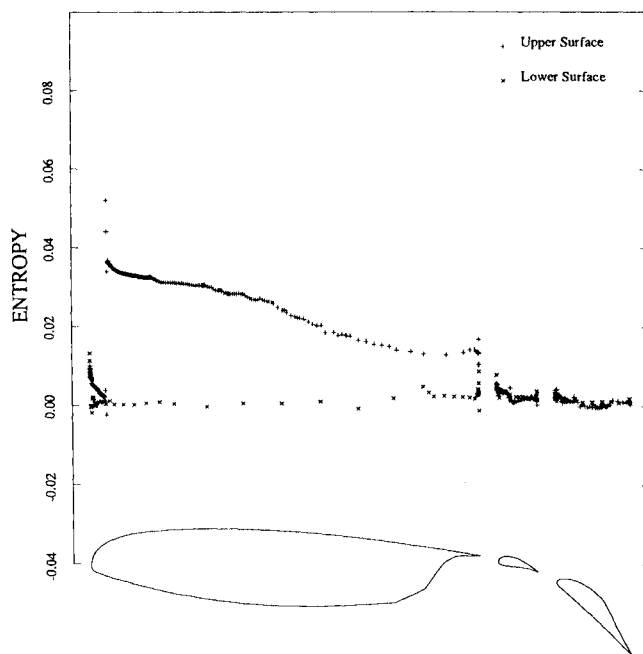

Fig. 20   Flowfield Mach contours for the supercritical three-element airfoil case (M = 0.25, incidence = 8 deg).

Fig. 19   Computed surface entropy distribution for the supercritical three-element airfoil case (M = 0.25, incidence = 8 deg).

Fig. 21   Mach contours near the leading edge of the main airfoil of the three-element configuration.

diffused due to the decreasing mesh resolution proceeding downstream in this region. Figures 20 and 21 also depict the Mach number contours in the flowfield. Although the extent of the shock is small, the Mach number ahead of it is 1.53 in the Euler solution, or 1.60 in the potential flow solution. In either case, this represents a strong shock, which cannot be accurately modeled by the potential flow assumption. The wide Mach number variation ahead of the shock results in a varying shock strength, and hence varying downstream entropy production. This normal gradient of entropy results in the generation of vorticity, and a shear layer along the top surface of the main airfoil is formed. This shear layer is reflected in the nearly horizontal Mach contours in this region,
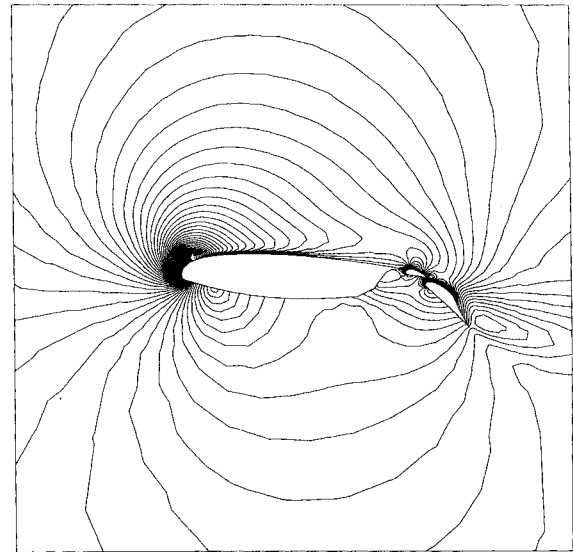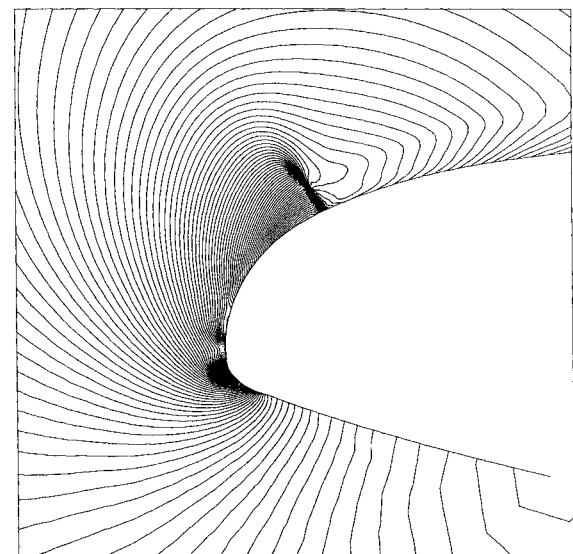
as observed in Fig. 20. Although there are some discrepancies between the two solutions on the main airfoil, the largest differences occur on the upper surfaces of the vane and flap. This is surprising, since the entirety of the flow that impinges upon the vane and the flap originates from the lower surface of the main airfoil, as it is channeled through the gaps. It appears that the shear layer produced by the shock, which is not present in the potential solution, has a global effect on the entire flowfield. On the other hand, the numerical diffusion of this shear layer, which enables it to impinge slightly upon the vane and flap, may contribute to these discrepancies. However, from Fig. 19, the surface entropy is seen to be much less than 1% everywhere except in the shear layer behind the shock, on the main airfoil. Furthermore, the same characteristic discrepancies between the two solutions were noted when alternate meshes were employed for the Euler solution. Increased mesh resolution in the region of the shear layer would be desirable to further limit the diffusion of entropy.

Conclusion

An accurate and efficient method for solving the Euler equations about complex geometries has been demonstrated. The method requires approximately 0.12×10^{-3} s/node/mg-cycle on the CRAY-2 supercomputer. Thus, the results about simple geometries presented in this work required 1–2 min of CPU time, whereas the three-element airfoil calculations were obtained in about 6–8 min. The present code can be expected to run substantially faster on a CRAY-XMP class machine, due to the more efficient gather-scatter routines available. Good agreement with other available inviscid solutions has been demonstrated. For supercritical flow over the three-element high-lift configuration, discrepancies between the present Euler solution and the full-potential solution of Ref. 16 exist, the origin of which appears to be related to the presence of a shear layer behind the shock, which cannot be captured by a full-potential method. Future work is aimed at further optimizing the efficiency of the method by implementing a directional refinement strategy. The inclusion of viscous effects by solving the Reynolds-averaged Navier-Stokes equations is also planned.

References

[1]Jameson, A., Baker, T. J., and Weatherill, N. P., "Calculation of Inviscid Transonic Flow over a Complete Aircraft," AIAA Paper 86-0103, Jan. 1986.

[2]Stoufflet, B., Periaux, J., Fezoui, F., and Dervieux, A., "Numerical Simulation of Three-Dimensional Hypersonic Euler Flows Around Space Vehicles Using Adapted Finite Elements," AIAA Paper 87-0560, Jan. 1987.

[3]Lohner, R., Morgan, K., Peraire, J., and Vahdati, M., "Finite-Element Flux-Corrected Transport for the Euler and Navier-Stokes Equations," ICASE Rept. No. 87-4, NASA CR-178233, Jan. 1987.

[4]Thompson, J. F., "Composite Grid Generation for General Three-Dimensional Regions," *Proceedings of the International Conf. on Numerical Grid Generation in Computational Fluid Dynamics,* Landshut, West Germany, July 1986, pp. 271–290.

[5]Usab, W. J. and Murman, E. M., "Embedded Mesh Solution of the Euler Equations Using a Multiple Grid Method," AIAA Paper 83-1946-CP, July 1983.

[6]Mavriplis, D. J., "Multigrid Solution of the Two-Dimensional Euler Equations on Unstructured Triangular Meshes," *AIAA Journal,* Vol. 26, No. 7, July 1988, pp. 824–831.

[7]Mavriplis, D. J. and Jameson, A., "Multigrid Solution of the Euler Equations on Unstructured and Adaptive Meshes," ICASE Rept. No. 87-53, NASA CR-178346, July 1987.

[8]Roe, P. R., "Error Estimates for Cell-Vertex Solutions for the Compressible Euler Equations," ICASE Rept. No. 87-6, NASA CR-178235, Jan. 1987.

[9]Mavriplis, D., "Solution of the Two-Dimensional Euler Equations on Unstructured Triangular Meshes," Ph.D. Thesis, Princeton Univ., Princeton, NJ, June 1987.

[10]Lindquist, D. R., "A Comparison of Numerical Schemes on Triangular and Quadrilateral Meshes," Master's Thesis, M.I.T., Cambridge, MA, May 1988.

[11]Jameson, A., Schmidt, W., and Turkel, E., "Numerical Solutions of the Euler Equations by Finite-Volume Methods Using Runge-Kutta Time Stepping Schemes," AIAA Paper 81-1259, June 1981.

[12]Van Leer, B., Thomas, J. L., Roe, P. L., and Newsome, R. W., "A Comparison of Numerical Flux Formulas for the Euler and Navier-Stokes Equations," AIAA Paper 87-1104, June 1987.

[13]Thomas, J. L. and Salas, M. D., "Far-Field Boundary Conditions for Transonic Lifting Solutions to the Euler Equations," AIAA Paper 85-0020, Jan. 1985.

[14]Pulliam, T. H. and Barton, J. T., "Euler Computations of AGARD Working Group 07 Airfoil Test Cases," AIAA Paper 85-0018, Jan. 1985.

[15]Dannenhoffer, J. F. and Baron, J. R., "Grid Adaptation for the Two-Dimensional Euler Equations," AIAA Paper 85-0484, Jan. 1985.

[16]Wigton, L. B., Private communication, 1987.